Volume 10, Number 2 (April 2017) p. 477 - 508 • ISSN 1983-4195
http://dx.doi.org/10.1590/S1983-41952017000200010

REVISTA IBRACON DE ESTRUTURAS E MATERIAIS
IBRACON STRUCTURES AND MATERIALS JOURNAL

Numerical and experimental evaluation of masonry prisms by finite element method

Avaliação numérico-experimental de prismas de alvenaria estrutural pelo método dos elementos finitos







C. F. R. SANTOS [a]
carolrezende@usp.br

R. C. S. S. ALVARENGA [b]
rcassia.alvarenga@gmail.com

J. C. L. RIBEIRO [b]
jcarlos.ribeiro@ufv.br

L. O. CASTRO [b]
lucascastro.ecivil@gmail.com

R. M. SILVA [c]
roberto@dees.ufmg.br

A. A. R. SANTOS [d]
alexrezendeufv@gmail.com

G. H. NALON [b]
gustavohnalon@gmail.com

Abstract

This work developed experimental tests and numerical models able to represent the mechanical behavior of prisms made of ordinary and high strength concrete blocks. Experimental tests of prisms were performed and a detailed micro-modeling strategy was adopted for numerical analysis. In this modeling technique, each material (block and mortar) was represented by its own mechanical properties. The validation of numerical models was based on experimental results. It was found that the obtained numerical values of compressive strength and modulus of elasticity differ by 5% from the experimentally observed values. Moreover, mechanisms responsible for the rupture of the prisms were evaluated and compared to the behaviors observed in the tests and those described in the literature. Through experimental results it is possible to conclude that the numerical models have been able to represent both the mechanical properties and the failure mechanisms.

Keywords: numerical simulation, concrete prisms, prisms failure modes.

Resumo

No presente trabalho desenvolveram-se ensaios experimentais e modelos numéricos capazes de representar o comportamento mecânico de prismas confeccionados com blocos de concreto comuns e de alta resistência. Foram realizados ensaios experimentais de prismas e, para a análise numérica, adotou-se como estratégia de modelagem, a micromodelagem detalhada, onde cada material (bloco e argamassa) foi representado por suas propriedades mecânicas. A validação dos modelos numéricos foi realizada com base em resultados experimentais realizados. Verificou-se que os valores obtidos numericamente de resistência à compressão e módulo de elasticidade diferem 5% em relação aos valores observados experimentalmente. Ainda foram avaliados quais os mecanismos responsáveis pela ruptura dos prismas, comparando-se tanto com o comportamento verificado nos ensaios, quanto com os descritos na literatura. Por meio dos resultados experimentais conclui-se que os modelos numéricos foram capazes de representar tanto as propriedades mecânicas quanto os mecanismos responsáveis pela ruptura.

Palavras-chave: simulação numérica, prismas de concreto, modos de ruptura prismas.

[a] *Escola de Engenharia de São Carlos, São Carlos, SP, Brasil;*
[b] *Universidade Federal de Viçosa, Viçosa, MG, Brasil;*
[c] *Professor Titular, Universidade Federal de Minas Gerais, MG, Belo Horizonte, Brasil;*
[d] *Universidade Federal de Lavras, Viçosa, MG, Brasil.*

Received: 02 Jun 2016 • Accepted: 30 Ago 2016 • Available Online: 17 Apr 2017

1. Introduction

Masonry structure is a building system with elements that perform both structural and sealing functions, thus allowing a greater rationalization. As this system has been increasingly used in the construction sector, there is a need for innovative materials in the industry.

According to (Castro [1]), the use of minerals (silica fume, calcined clay) and plasticizing admixtures has proportioned blocks of greater strength and lower permeability, thus named high strength blocks. Despite the development of new materials and the use of much more slender structures, codes have not undergone many changes to follow such a big development. The main reason is the lack of experimental and mathematical models that explain the complex behavior of units and mortar working together as a composite material.

As an experimental program with wall testing is expensive, most of the authors agree that is possible to establish a relation between the load and failure mode of the walls, studying the prisms behavior. It would allow the reduction of testing costs. Still regarding the possibility of cost reduction, an alternative widely used to study specific phenomena is the numeric simulation. Since well calibrated, it is able to supply information about the structural behavior and provides subsidy to determine, with safety, the parameters to be used in project/codes.

In order to obtain a reliable and accurate numerical model, a complete description of the material must be made based on experimental results. Once calibrated the model, it is possible to vary the desired parameters and verify the isolated effect of each component. According to (Oliveira [2]), mortar joints represent planes of weakness and are responsible by most of the nonlinear phenomena that occur on the structure, which behavior makes the computer modeling process more complex.

Considering this context, the goal of this work is to present the calibration of prisms' numerical models, based on the experimental results obtained by (Oliveira [2]) and also by the authors of this work. With the numerical modeling results, a study will be conducted to compare the mechanisms responsible by failure to the behavior observed during the tests.

2. Context

In order to base the discussion of the results (item 4), some conclusions about prisms obtained by other researchers will be presented.

2.1 Behavior of mortar in the prisms

When the masonry is submitted to a vertical loading, the generated state of stress causes horizontal stresses on the mortar joint due to existing adhesion between the unit and the mortar. So, in a prism or wall, the mortar is subjected to a triaxial state of stress, presenting a behavior different from that observed in uniaxial testing. It is noted that when the mortar is subjected to a triaxial state of stress, changes occur in its mechanical properties, such as: compressive strength, Young's modulus, and Poisson's ratio. According to (Mohamad [3]) and (Khoo [4]), the study of the behavior of confined mortar is essencial to understand the failure mechanisms of prisms and walls, either by reaching the block's tensile strength, or occurring the block's localized crushing, or happening the mortar bed joints crushing. Thus, both authors studied the increase of mortar compressive strength due to the increase of the confining pressure, obtaining the failure envelope. The equations (1) and (2) correspond to the failure envelope proposed by (Mohamad [3]) and (Khoo [4]) to mortar 1:1:6, respectively.

$$f_{arg}* = f_{arg} + 2{,}6 \cdot f_{tm} \quad (1)$$

$$f_{arg}* = f_{arg} + 2{,}3 \cdot f_{tm} \quad (2)$$

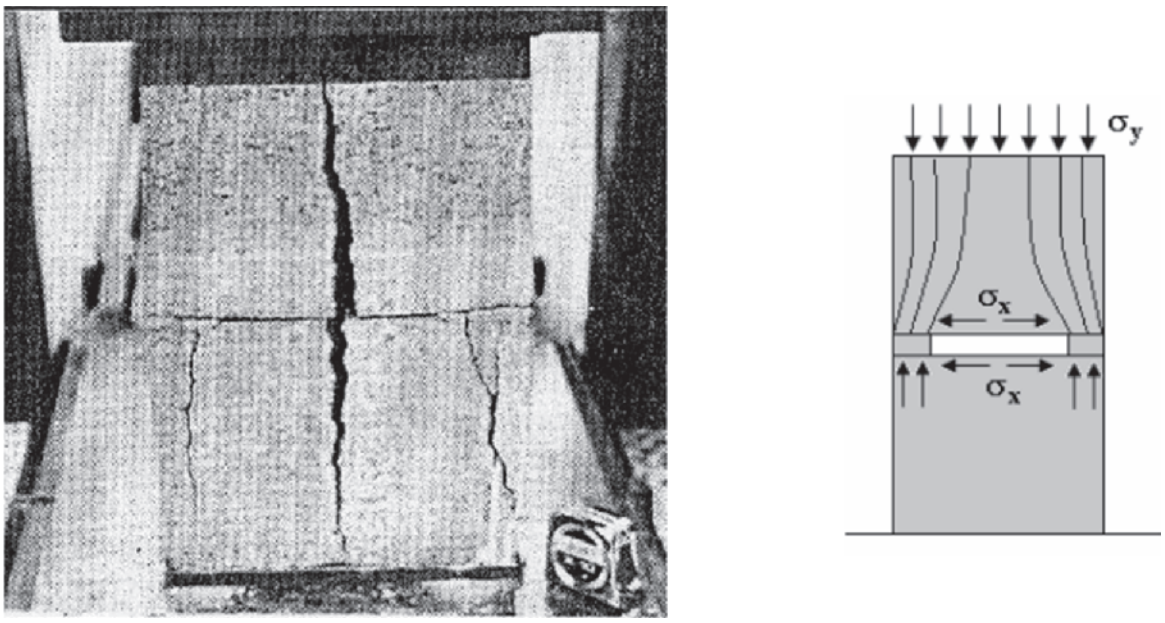

Figure 1
Rupture of concrete block prisms with face shell mortar bedding (Mohamad (3))

where:
f_{arg} * is the compressive strength of confined mortar;
f_{arg} is the uniaxial compressive strength of mortar;
f_{tm} is the lateral confining stress.

2.2 Shear strength of masonry mortar joint

The shear strength of the mortar joints has a behavior that can be described by Coulomb's law, which is given by equation (3), (Riddington [5]).

$$\tau_u = f_{vo} + tan\varphi \cdot \sigma \quad (3)$$

where:
τ_u is the shear strength of horizontal or vertical joint;
f_{v0} is the shear strength by initial adherence, also named cohesion;
σ is the normal pre-compression stress acting across the joint;
ϕ is the friction angle of the material.

2.3 Rupture modes of the prisms

There is a consensus among researchers that the rupture mode of prisms and walls is function of the mechanical properties of their constituent materials, such as Young's modulus and compressive strength. The studies led by (Hamid e Drysdale [6]) suggest that the mechanism of rupture of masonry occurs due to the biaxial tensile-compressive stress state, in consequence of the low stiffness of the mortar. According to the authors, the units prevent the lateral deformation of the mortar, resulting in lateral confining stresses on it, so the mortar strength is considerably increased. Analyzing the experimental results, the authors concluded that when the loads reach approximately 80% of the ultimate load, some microcracking occurs along the entire length of the prisms.
As done by other authors, (Mohamad [3]) performed experimental tests on prisms of concrete units with face shell mortar bedding. In the rupture, they observed the development of tensile stresses on the lateral face caused by rotation and crushing of the supports. This rupture mechanism is similar to the beams', in which the mortar's lateral crushing induces horizontal stresses that cause the material to fail in bending, as can be seen in Figure 1.
In his tests, (Romagna) [7] evaluated the mechanical behavior of concrete prisms under compression. The author noted the development of intense cracking at the intersection of the blocks' face shells and webs, and also crumbling at the block's surface. The author also reported that there were cracks in specific points of the block's walls due to the loss of mortar load-carrying capacity, causing the units' overlapping and their consequent crushing.

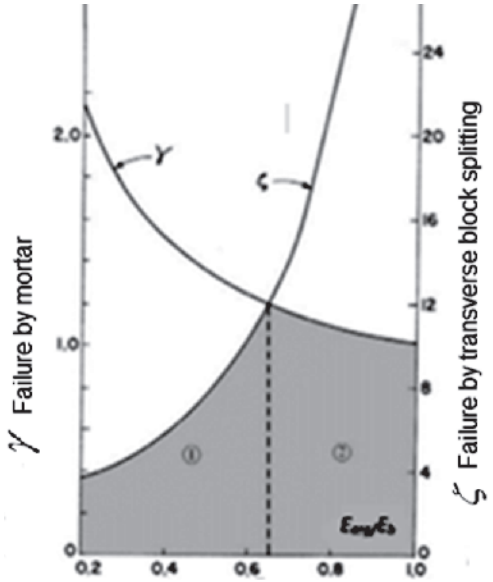

Figure 2
Curve of failure of ungrouted prisms, (Juste (9))

In this context, the research carried out by (Cheema e Klingner [8] apud Juste [9]) can be also mentioned. They developed mathematical expressions able to predict the compressive load related to the occurrence of each kind of rupture of ungrouted prisms (by transverse block splitting, block crushing or mortar crushing), depending on the relationship between the elasticity modulus of mortar and blocks. Based on some expressions it was possible to plot the graph shown in Figure 2. When $E_{arg}/E_b \geq 0.66$ the rupture occurs, preferably, by mortar crushing (region 2 of the Figure 2). When $E_{arg}/E_b \leq 0.66$ the rupture occurs by transverse block splitting (region 1 of the Figure 2).

3. Materials and methods

This paper performed a numeric simulation of some prisms tested by the authors of this work and others by (Oliveira [2]). In both cases, the prisms were produced using face shell mortar bedding and concrete blocks. The authors of this study used high strength blocks and (Oliveira [2]) used common blocks. For calibration and validation of

Table 1
Experimental results, Authors

Experimental data (Authors)							
Blocks*				Prism**		Mortar*	
Dimensions (cm)	f_{bm} (MPa)	E_{cm} (MPa)	$f_{tb,ind}$ (MPa)	f_{pm} (MPa)	E_{pm} (MPa)	f_m (MPa)	E_m (MPa)
15 x 19 x 29	35.19	35.37	1.76	10.60	8006.00	11.80	9293.05

* Results related to the net area; ** Data related to the gross area

Table 2
Experimental results, (Oliveira (2))

Experimental Data (Oliveira (2))							
Blocks*				**Prism****		**Mortar***	
Dimensions (cm)	f_{bm} (MPa)	E_{cm} (MPa)	$f_{tb,ind}$ (MPa)	f_{pm} (MPa)	E_{pm} (MPa)	f_m (MPa)	E_m (MPa)
14 x 19 x 39	18.65	18.10	0.91	4.49	8420.00	3.52	6800.00

* Results related to the net area; ** Data related to the gross area

numerical models the authors used the experimental results and the description of the rupture modes experimentally certified.

3.1 Materials

Table 1 and Table 2 present experimental results used in the construction and validation of the numerical models, obtained by the authors and (Oliveira [2]), respectively.
Figure 3ab presents the rupture modes displayed in the experimental tests performed by the authors and (Oliveira [2]), respectively.

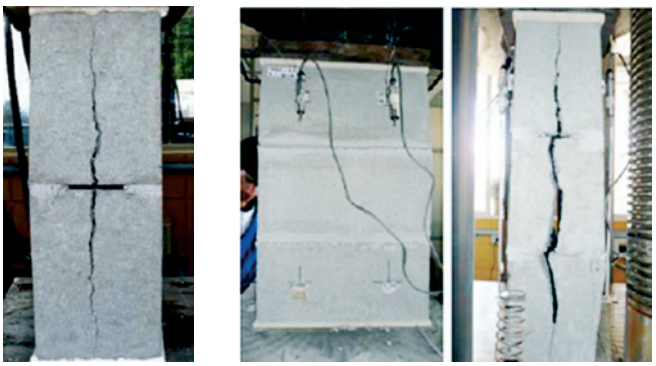

Figure 3
Failure mode of concrete block prisms, Authors and (Oliveira (2))

It should be emphasized that the commercial software ABAQUS was used to perform the numerical modeling, by Finite Element Method.

3.2 Methods

A detailed micro-modeling strategy was adopted for numerical modeling of the prisms. In this technique, each component of the prism was represented by its own mechanical properties and dimensions. It was also necessary to supply parameters for complete discrimination of block/mortar interface (item 3.5).

3.3 Description of the models

The finite element used to generate the mesh that represents blocks and mortar was C3D8, which is a solid element of eight nodes with linear interpolation and complete integration, able to represent the translations in x, y and z-axis, once the element has three degrees of freedom per node.
In order to facilitate the description of the numerical models, they were identified as PA and PO, which are related to the experimental results used for calibration and validation obtained by the present authors and (Oliveira [2]), respectively.
When performing meshing tests, it was decided to use, for PA model, elements with dimensions of 1 cm for the blocks and 5 mm for the mortar. For PO model, elements with 2 cm for the blocks and 5 mm for the mortar proved to be more appropriate. The meshing

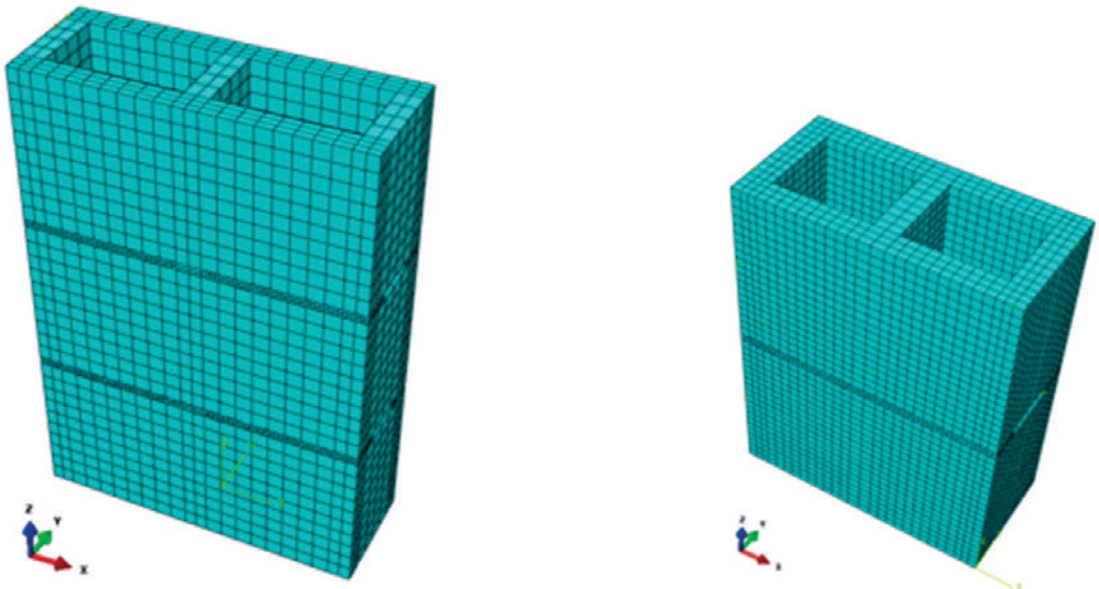

Figure 4
General aspects of the prism's mesh

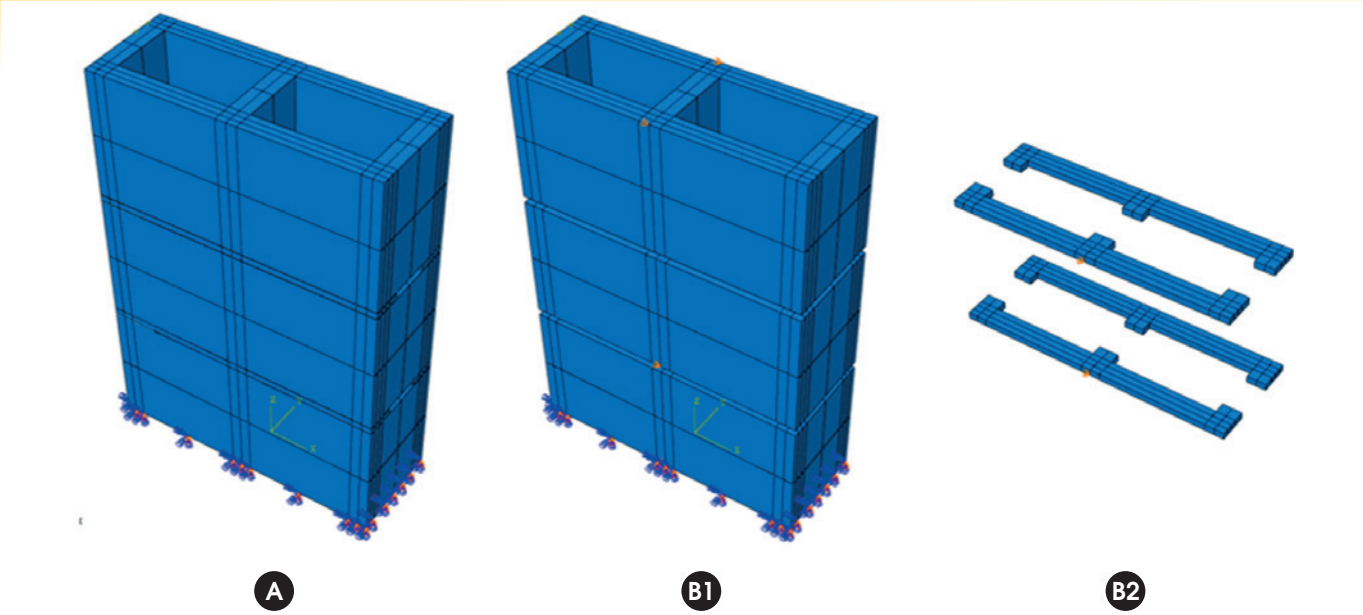

Figure 5
Boundary conditions of the prisms

difference between the two models occurs due to the lowest number of interfaces in the PA model, allowing further refinement of the block mesh, still having a reasonable computational cost. In Figure 4, the general aspects of the meshes of the models are presented.
In respect to the loading, it was decided to apply a prescribed displacement (1,0 cm) to the entire top surface, thus all nodes of the surface were subjected to a rigid body motion. The analysis method for the models was the *Static General, Newton Rapson.*
For the supports, both models have had the same boundary conditions, shown in Figure 5abc. They where: a) z-axis translational restraint at the base of the block, Figure 5a; b) x-axis displacement restraint for both block(1) and mortar(2), Figure 5b; c) y-axis displacement restraint for both block (1) and mortar (2), Figure 5c. Both x and y restraints of blocks and joints were imposed to all of the model's blocks and joints.

3.4 Constitutive model

The constitutive model used to represent the mechanical behavior of blocks and mortars was the Concrete Damaged Plasticity. According to (Kmiecik and Kaminski [10]), this model is an adaptation of the Drucker-Prager model, which is also used to represent the mechanical behavior of brittle materials.
In *Concrete Damaged Plasticity* (CDP), the equation that defines

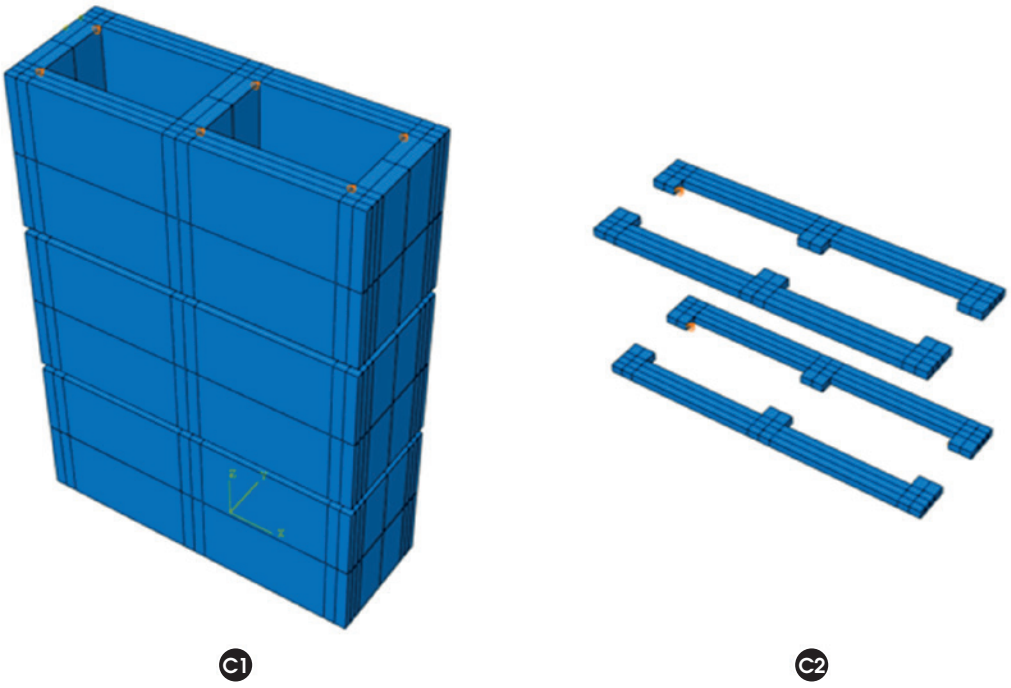

Figure 6
Continuation of the boundary conditions of the prisms

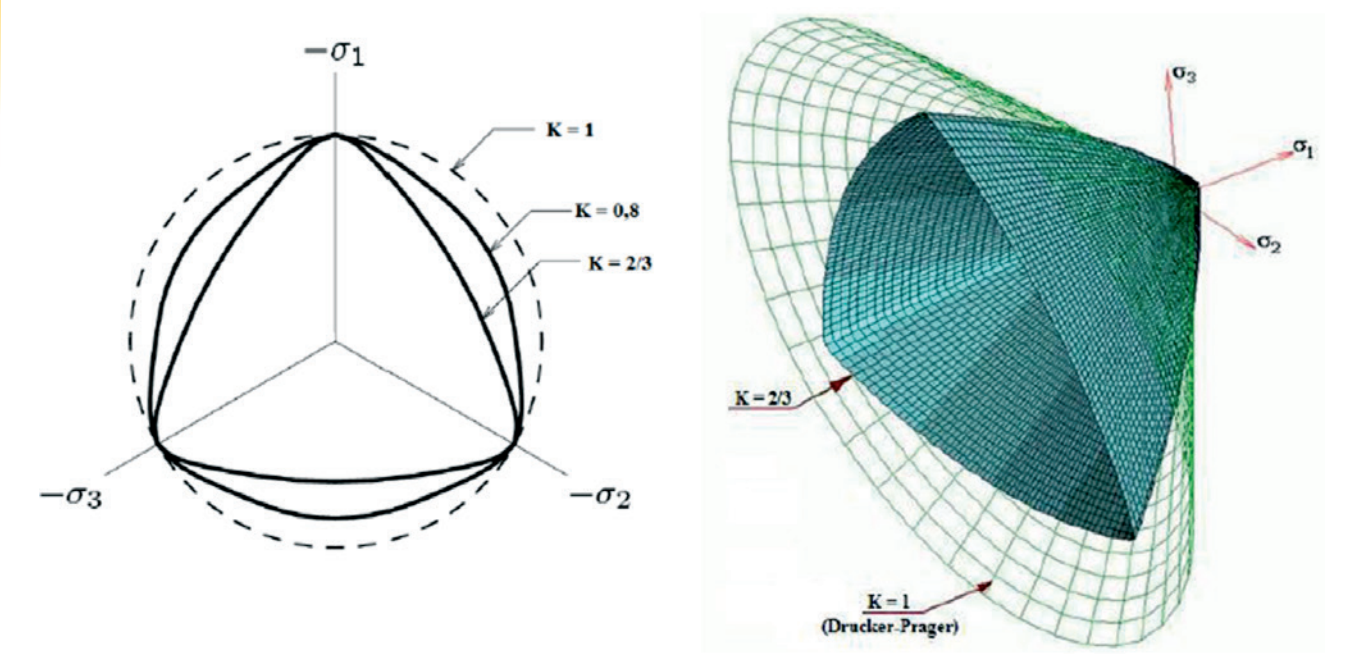

Figure 7
Influence of the K_c parameter on the shape of the yield surface.
Source: Aguiar (2014)

the surface of Drucker Prager is modified by a K_c parameter equal to 2/3, Figure 7. Note that this model has been proposed by (Lubliner *et al*. [11]).
Still about the constitutive model, it is necessary to define some essential calibration parameters to make it be useful:

3.4.1 Behavior under uniaxial compression in the inelastic region

In the CDP constitutive model, elastic and inelastic deformation (ε_{el} and ε_{inel}, respectively) are calculated independently, and subsequently summed to obtain the total deformation (ε). ε_{el} depends only on the materials' modulus of elasticity and Poisson's ratio and ε_{inel} is obtained from their stress-strain curve.
In many cases, it is difficult to obtain stress-strain curves experimentally. Some authors and codes present empirical formulations, in which the researcher only includes parameters that are generally easy to determine.
The compression's stress-strain curve used in this paper was proposed by (Guo [12]). It considers the elastic region until 30% of the ultimate load, where the modulus of elasticity is the slope of the stress-strain diagram. The inelastic region is defined by the formulation proposed by (Guo [12]). Figure 8 presents his schematic stress-strain curve.
As described above, the curve is composed by two regions. The formulation that composes each region is given by equations (4), (5),(6),(7),(8) e (9):
- Elastic region:

$$\sigma_c = E_{cm} \cdot \varepsilon \tag{4}$$

- Inelastic region:

$$\sigma_c = f_{bm} \cdot [\alpha_a x + (3 - 2\alpha_a)x^2 + (\alpha_a - 2)\, x^3] \quad x \le 1 \tag{5}$$

$$\sigma_c = \frac{f_{bm}}{\alpha_d (x-1)^2 x} \quad x > 1 \tag{6}$$

where:

$$x = \frac{\varepsilon}{\varepsilon_{c1}} \tag{7}$$

$$\alpha_a = \frac{E_{cm}}{E_{c1}} \tag{8}$$

$$1.5 \le \alpha_d \le 3 \tag{9}$$

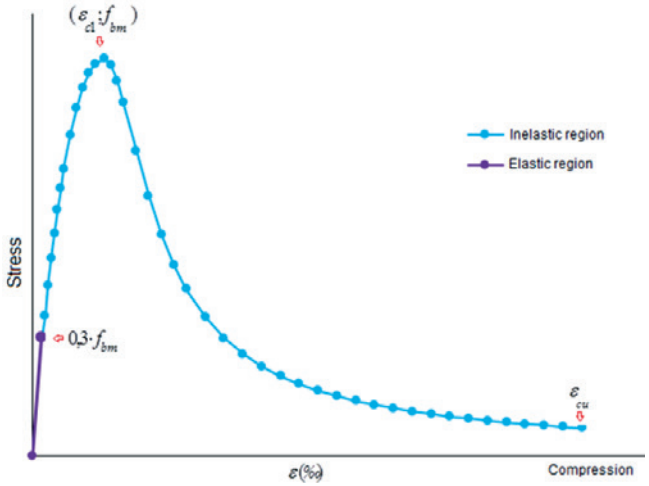

Figure 8
Behavior of concrete under compression, generic curve

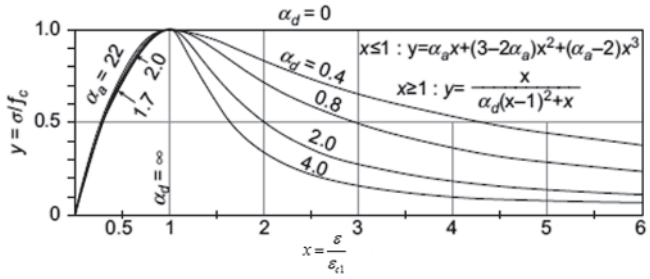

Figure 9
Parameter range
Source: Guo (2014)

and:
- E_{cm} is the initial modulus of elasticity (considering a stress of 0,3 f_{bm});
- E_{c1} is the secant modulus of elasticity (considering the maximum stress).

The parameter α_d affects the descendant portion of the curve, as shown in Figure 9, and must be calibrated.

The program requires the portion of deformation of the stress-strain curve related to the inelastic deformation independently. Then, it is necessary to subtract the elastic deformation of the total deformation, by using the equation (10):

$$\varepsilon_{inel} = \varepsilon - \frac{\sigma_c}{E_{cm}} \quad (10)$$

Applying this equation to calculate a new deformation for each point of the described stress-strain curve, it is possible to build the curve that supplies the software, Figure 10.

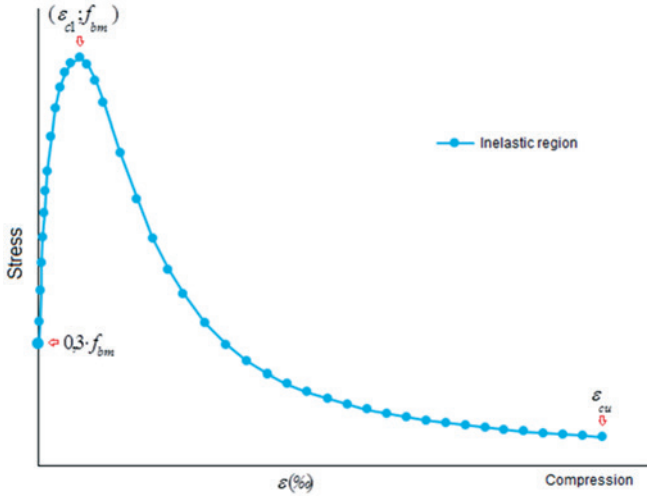

Figure 10
Stress-inelastic strain curve, generic curve

The parameters values necessary to build the analytical stress-strain curve of blocks and mortar are shown in Table 3 and Table 4. The values of α_d were obtained from the experimental curves obtained by (Oliveira [2]). For the experimental curves obtained in this study, the same α_d obtained by (Oliveira [2]) was adopted.

3.4.2 Behavior under uniaxial tensile in the inelastic region

As done for compression, it is necessary to indicate the behavior of the material under tensile. Thus, it is necessary to provide the tensile's stress-strain curve, that also has an elastic and an inelastic portion, (Guo [12]), Figure 11. The elastic region is described by

Table 3
Input parameters for stress-strain curve, (Oliveira (2))

(Oliveira (2))									
Blocks*					Mortar				
f_{bm} (MPa)	E_{cm} (MPa)	α_d	ε_{c1} (‰)[1]	ε_{cu} (‰)	f_{bm} (MPa)	E_{cm} (MPa)	α_d	ε_{c1} (‰)[1]	ε_{cu} (‰)
18.64	18115.0	2.3	2.24	30	3.52	6796.7	0.4	1.883	10
* Block properties related to the net area; [1] the strain at peak load was determined based on the stress-strain curve experimentally obtained.									

Table 4
Input parameters for stress-strain curve, Authors

Authors									
Blocks*					Mortar				
f_{bm} (MPa)	E_{cm} (MPa)	α_d	ε_{c1} (‰)[1]	ε_{cu} (‰)	f_{bm} (MPa)	E_{cm} (MPa)	α_d	ε_{c1} (‰)[1]	ε_{cu} (‰)
35.37	35459.14	2.3	2.3	30	11.80	9293.05	0.4	1.9	30
* Block properties related to the net area; [1] the strain at peak load was determined based on the values suggested by Fib Bulletin 65: Model Code 2012 (16).									

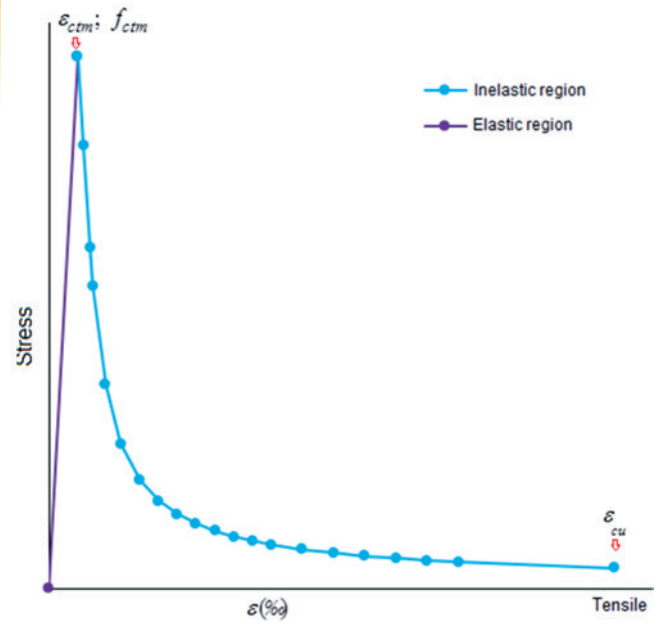

Figure 11
Stress-inelastic strain curve, tensile generic curve

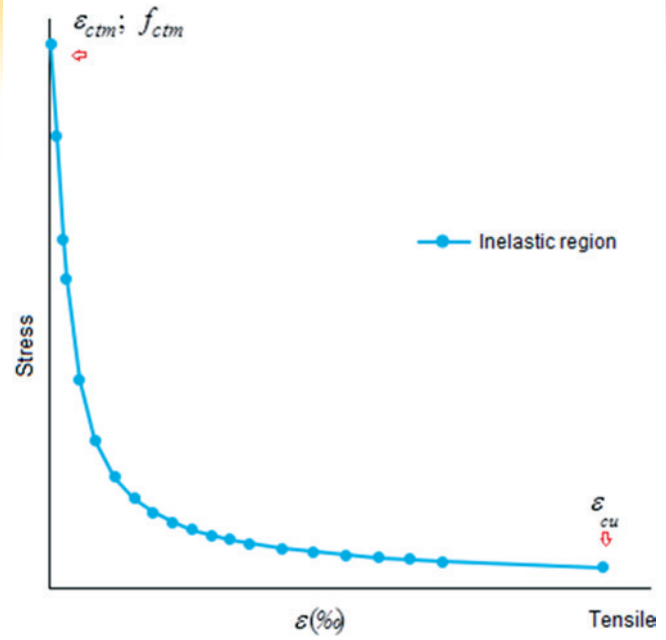

Figure 12
Stress-inelastic strain curve, tensile generic curve

equation (11) and the inelastic deformation is described by equations (12), (13), (14) e (15).
- Elastic region:

$$f_{btm} = E_{cm} \cdot \varepsilon \quad (11)$$

-Inelastic region:

$$\sigma_t = f_{btm} \frac{x}{\alpha_t \left[x-1\right]^{1,7} + x} \quad (12)$$

where:

$$\alpha_t = 0.312 \cdot f_{btm} \quad (13)$$

$$x = \frac{\varepsilon}{\varepsilon_{ct}} \quad (14)$$

$$\varepsilon_{ct} = \frac{f_{btm}}{E_{cm}} \quad (15)$$

and:
- E_{cm} is the initial tangent modulus of elasticity;
- f_{btm} is the tensile strength of material.
For concrete, the (ABNT NBR 6118:2014 [17]) estimates the tensile strength as $f_{ctm} = 0.3 \cdot (f_{ck})^{2/3}$. However, there is no specification for tensile strength of blocks and mortar. Then, equation (16) was adopted:

Table 5
Input parameters for tensile stress-strain curve, (Oliveira (2))

(Oliveira (2))							
Blocks*				Mortar			
f_{btm} (MPa)	E_{cm} (MPa)	ε_{c1} (‰)[1]	ε_{cu} (‰)	f_{at} (MPa)	E_{cm} (MPa)	ε_{c1} (‰)[1]	ε_{cu} (‰)
2.11	18115.1	0.1164	0.9	0.7	6796.7	0.1021	0.9
* Block properties related to the net area.							

Table 6
Input parameters for tensile stress-strain curve, Authors

Authors							
Blocks*				Mortar			
f_{btm} (MPa)	E_{cm} (MPa)	ε_{c1} (‰)[1]	ε_{cu} (‰)	f_{at} (MPa)	E_{cm} (MPa)	ε_{c1} (‰)[1]	ε_{cu} (‰)
3.23	35459.14	0.0912	0.9	1.97	9293	0.2	0.9
* Block properties related to the net area.							

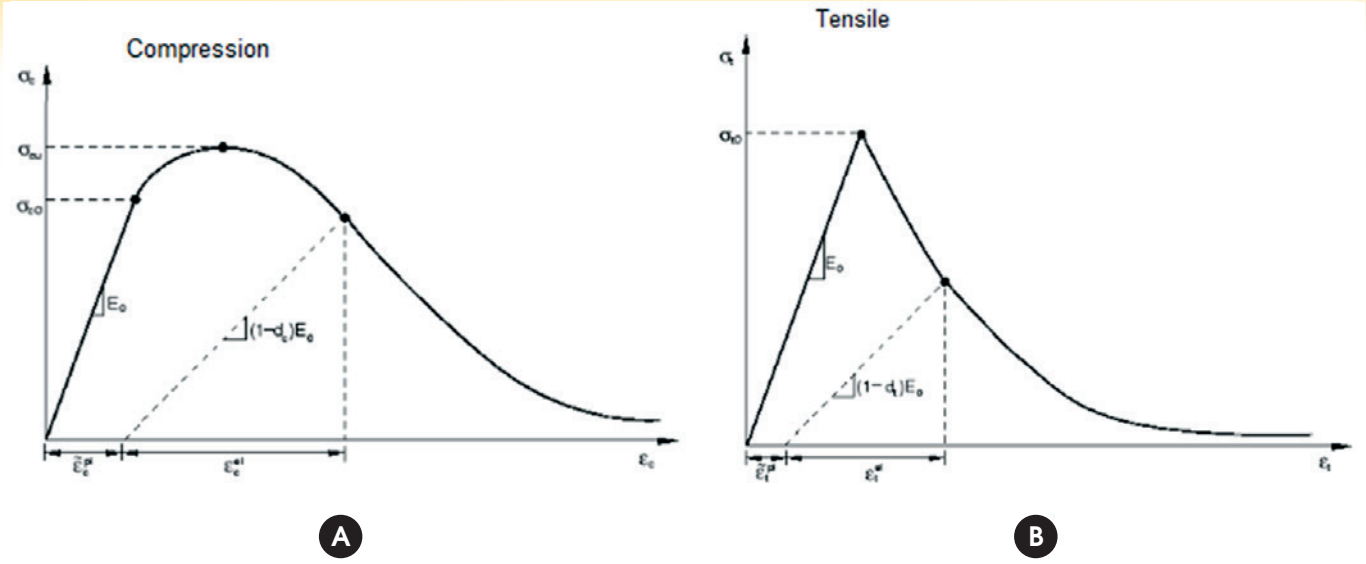

Figure 13
Degradation of the material's stiffness, SIMULIA (13)
Source: Simulia (2012)

$$f_{btm} = 0.3 \cdot (f_{bm})^{2/3} \quad (16)$$

As done for compression, it is necessary to calculate the portion of deformation related to the inelastic one, in order to build the stress-strain curve shown in (Figure 11). Again, the elastic deformation was subtracted of the total deformation, as done to obtain equation (10). The input parameters used in the modeling are presented in Table 5 and Table 6.

3.4.3 Stiffness degradation of the material

When applied the load and exceeded the elastic region, a stiffness degradation occurs due to the appearance of plastic deformation. This degradation can be determined by unloading the material, calculating the unloading modulus of elasticity, and comparing it to the initial modulus of elasticity. As a simplification, it was assumed that this behavior occurs just in the postpeak stress–strain curve, Figure 13.

The decrease of the slope is ruled by two independent variables, d_c (damage in uniaxial compression) and d_t (damage in uniaxial tensile). It ranges from zero for an undamaged material to one for the total loss of load-bearing capacity. According to (Cardoso [14]), those variables can be defined using the equations (17) and (18):

$$d_c = 1 - \frac{\sigma_c}{f_{bm}} \quad (17)$$

$$d_t = 1 - \frac{\sigma_t}{f_{ctm}} \quad (18)$$

3.4.4 Parameters of the constitutive model Concrete Damaged Plasticity

Besides the previously mentioned parameters, it is necessary to provide to ABAQUS some other ones, which are responsible for allowing to apply the equations of the behavior of materials under uniaxial state of stress to materials under multiaxial state of stress (Aguiar [15]):

- $\sigma_{b0} / \sigma_{c0}$: Parameter that describes the ratio between the yield strength in biaxial and uniaxial state. This study adopted the value of 1.16 given by ABAQUS, (SIMULIA [13]) as a default value.
- Dilation angle (ψ) : According to (Cardoso [13]), this parameter is related to the slope that the plastic potencial reaches under higher confining stress. (Kmiecik and Kaminski [10]) define the dilation angle as the concrete's angle of internal friction and recommend the adoption of $\psi = 36°$.
- Viscosity parameter (μ) : Parameter whose function is facilitate process of numerical models, regulating the constitutive equations through the viscoplasticity study. In this work, a value of $\mu = 10^{-6}$ was adopted, based on a preliminary study that looked for the lower value of viscoplasticity that facilitated the convergence process, without affecting the results.
- Eccentricity parameter ρ : According to the theory of Drucker Prager, the yield surface in the meridian planes has the form of a straight line ($\rho = 0$). However, the experimental trials indicate that the yield surface takes the shape of a hyperbole close to the hydrostatic axis ($\rho = 0.1$). In this study, it was adopted $\rho = 0$.

3.5 Description of the block/mortar interface

To make block and mortar interact together in the model, it was necessary to define the relationship between them. The *Interactions* module of ABAQUS was used to do this. The contact between the surfaces was established through the option called surface-to-surface contact, where three contact properties were defined: *Hard, Tangential Behavior, Cohesive Behavior and Damage*.

- The *Hard* contact has the ability to prevent a surface penetrates other surface and also allows a separation between them, after the contact is established.
- The *Tangential Behavior* contact can reproduce the friction that occurs on the connection between the materials. It is defined by the static friction coefficient ϕ. It obeys the Coulomb law, in which the shear strength increases due to the increase of the compression

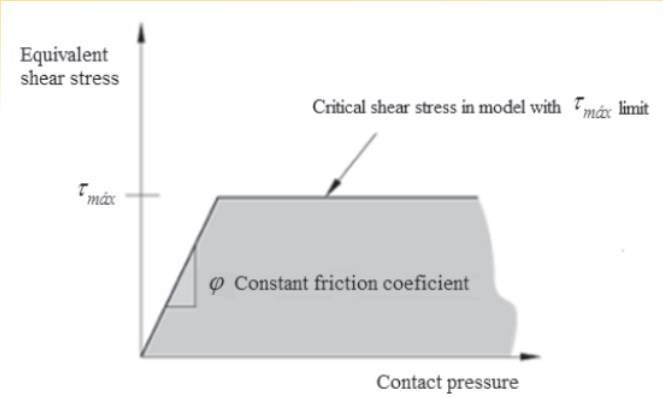

Figure 14
Tangential Behavior, SIMULIA (13)
Source: Simulia (2012)

stress. Two features in this contact must be taken into consideration: the first one is that part of the cohesion is despised, and the second one is the possibility of establishing a critical shear stress $\tau_{máx}$. When the shear stress reaches this critical value, the slipping between the surfaces will occur without an increase in shear strength, regardless of the magnitude of the compressive stress, Figure 14.

- The *Cohesive Behavior* works like a zero thickness rubber, for which you can specify the normal stiffness K_{nn} and the tangential stiffness K_{ss}, K_{tt} of the interface. This kind of contact causes a stiffness degradation called Damage, in which it is only necessary to provide the interface's fracture energy.

The input parameters to define the interface properties are presented in Table 7 and Table 8.

The interfaces locations on the prisms models are shown in Figure 15ab and Figure 16ab. The positions of the interfaces were defined from the experimental results, and correspond to those where the cracks occured.

4. Results and discussion

4.1 Compressive strength and modulus of elasticity

The results obtained from the numerical models are presented below and compared to the experimental results presented at the item 3.1. Once the numeric models are validated for each case, the possible failure modes will be discussed. The properties of blocks and mortars used in the numerical modeling of the prisms were obtained from the mechanical characterization experimentally performed.

Remembering the convention used to identify the numerical model: PO is related to the numerical modeling of the prisms tested by (Oliveira [2]) and PA is related to the modeling of the prisms tested by the authors of this paper.

In Table 9 and Table 10, comparisons between experimental and numerical results of the (Oliveira [2]) and this authors' prisms are presented. The data include values for uniaxial compressive stresses and modulus of elasticity, calculated between 0.5 MPa and 30% of the failure load.

It is noted from Table 9 and Table 10 that the numerical models of the prisms represented well the mechanical behavior obtained experimentally for both failure mode and modulus of elasticity. The biggest difference between experimental and numerical results was around 5%. However, it is worthwhile to also make a comparison of the failure modes in order to verify the behavior compatibility between the experimental and numerical model. The principal stresses state at the moment of the rupture will be checked.

4.2 Principal stresses in the blocks

Figure 17ab shows the maximum principal stresses state that was acting (only on the blocks) at the time of the rupture, for the models PO and PA.

Figure 17a and Figure 17b show that, at the time of the rupture, the indirect tensile stress (related to the net area) experimentally obtained (0.91 MPa for blocks of this authors and 1.47 MPa for [2]) had already been exceeded. This behavior was mainly noted at the blocks' face shells, which were subjected to bending due to the face shell mortar bedding. Such behavior was also demonstrated in the experimental tests, according to the authors and [2].

Based on the Figure 17ab, at the time of the rupture, the blocks' face shells supported tensile stresses higher than the indirect tensile stresses of the blocks. This behavior is due to the stress generated by the tendency of expulsion of the mortar's outer edges (due to the vertical load), so that the shear strength between blocks and mortar was not exceeded, due to the friction between them. In the

Table 7
Input parameters adopted to define the interface properties, (Oliveira (2))

(Oliveira (2)) – Interface properties								
Tangential behavior		Cohesive behavior – N/m			Damage initiation – MPa			Damage evolution
φ	τ_{max} (MPa)	K_{nn}	K_{ss}	K_{tt}	$t_n°$	$t_s°$	$t_t°$	E_f (Nm)
0.5	10.5	5000	$2.1\ 10^6$	$2.1\ 10^6$	0.91	0.23	0.23	50

Table 8
Input parameters adopted to define the interface properties, Authors

(Authors) – Interface properties								
Tangential behavior		Cohesive behavior – N/m			Damage initiation – MPa			Damage evolution
φ	τ_{max} (MPa)	K_{nn}	K_{ss}	K_{tt}	$t_n°$	$t_s°$	$t_t°$	E_f (Nm)
0,5	10,5	5000	$2,1\ 10^6$	$2,1\ 10^6$	1,47	0,23	0,23	50

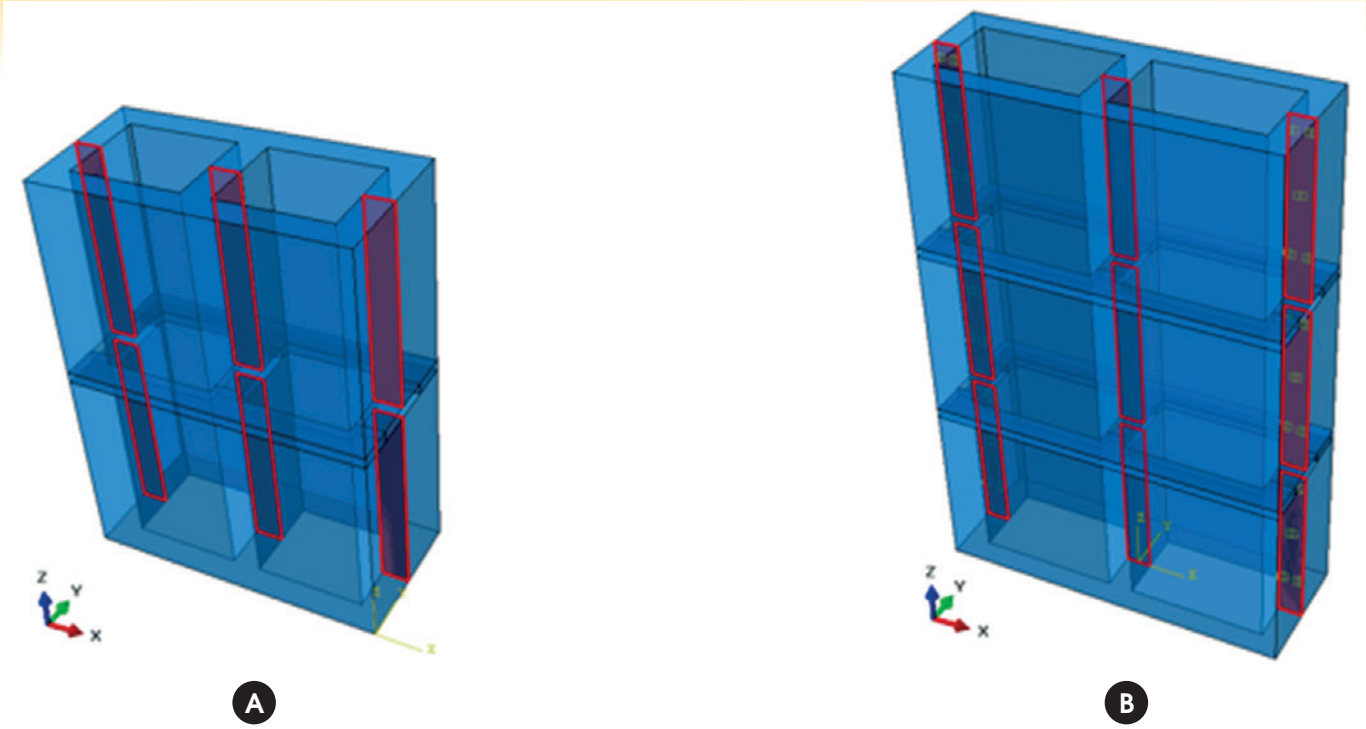

Figure 15
Location of the interfaces with Coesive Behavior

outer part of the mortar joint, the confining effect is smaller. Consequently, the mortar tends to present a greater deformation, causing the described effect. In this study, the occurrence of rupture of the block's walls was observed during the tests, thus indicating those tensile effects.

Figure 18ab presents the minimum principal stress state that was acting in the blocks at the time of the rupture, for the models PO e PA.

Based on Figure 18a and Figure 18b, at the time of the rupture, the lowest block's minimum principal stress have already presented values close to those obtained in the uniaxial compression test and related to the block's net area (18.64 MPa to PO and 35.37 MPa to PA). In both models, the blocks' face shells presented stresses close to their compressive strength, which indicates that the loads tend to concentrate in there. In the experiments performed

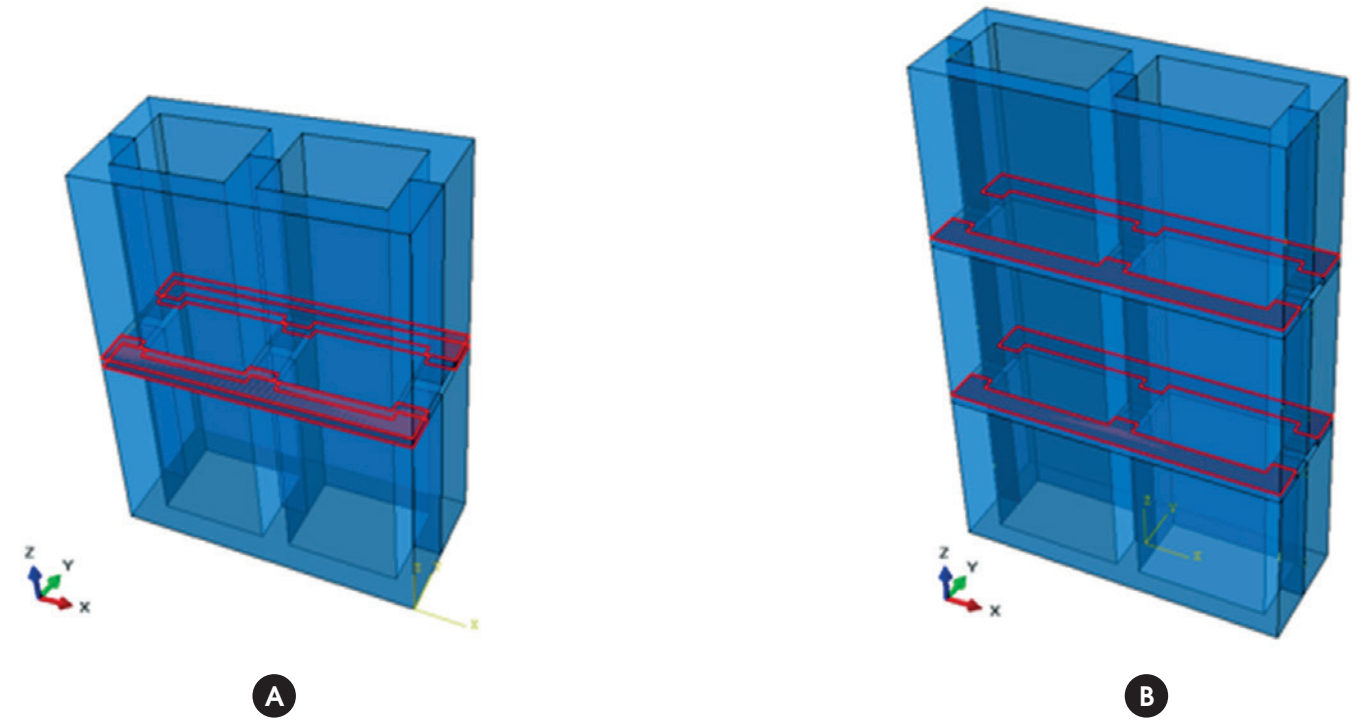

Figure 16
Location of the interfaces with Tangential Behavior and Hard contact

Table 9
Comparison between experimental and numerical results, PO

Comparison between experimental results obtained by (Oliveira (2)) and numerical ones obtained by the authors				
ID	Prisms compressive strength (f_p) MPa**	Modulus of elasticity (GPa)**	Prisms compressive strength (f_p) MPa***	Modulus of elasticity (GPa)***
PO – Exp.	5.16	8.17	9.42	14.92
PO – Num.	5.02	7.97	9.17	14.55
Difference %[1]	- 3%	- 3%	- 3%	- 3%

** Results related to the gross area; *** Results related to the net area; [1] Related to the experimental results.

Table 10
Comparison between experimental and numerical results, PA

Comparison between experimental and numerical results obtained by the authors				
ID	Prisms compressive strength (f_p) MPa**	Modulus of elasticity (MPa)**	Prisms compressive strength (f_p) MPa***	Modulus of elasticity (GPa)***
PA – Exp.	10.60	8006.40	18.47	13948.43
PA – Num.	10.11	7790.80	17.61	13572.82
Difference %1	- 5%	- 3%	- 5%	- 3%

** Results related to the gross area; *** Results related to the net area; [1] Related to the experimental results.

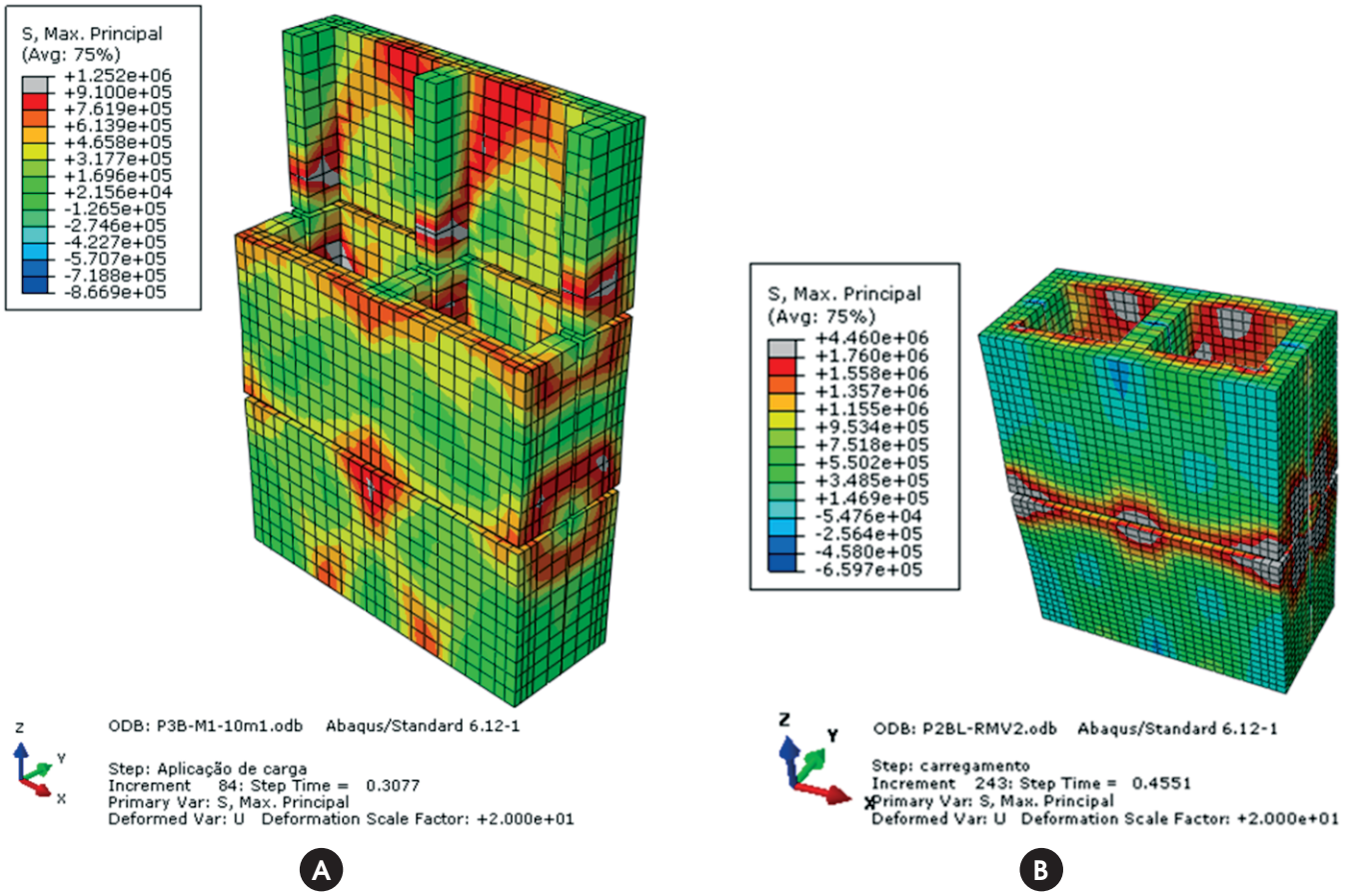

Figure 17
Maximum principal stress numerically obtained, in Pa – only blocks: a) PO model; b) PA model

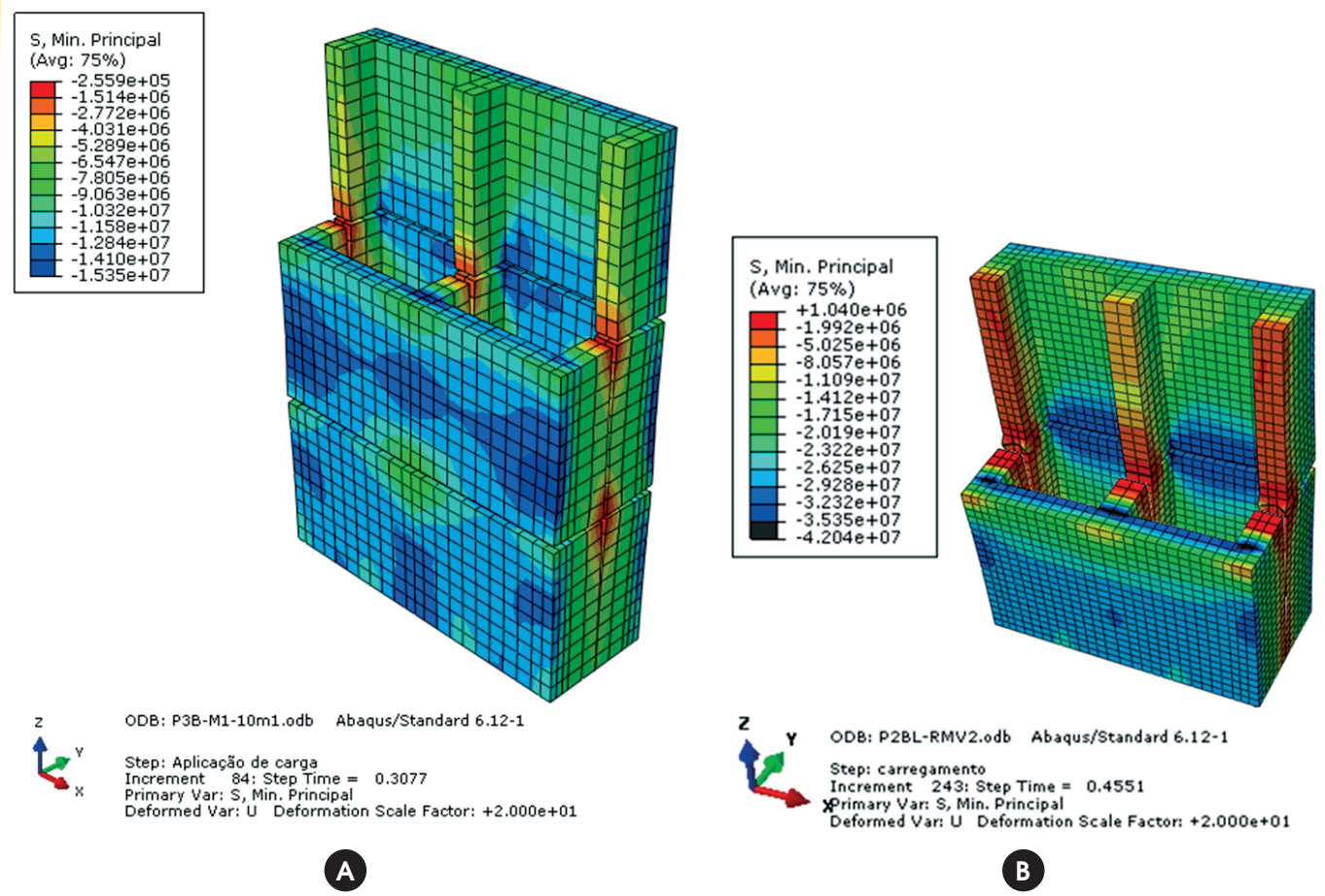

Figure 18
Minimum principal stress numerically obtained, in Pa – only blocks: a) PO model; b) PA model

by the authors, immediately after the peak load, intense cracking occurred on the blocks' face shells, causing their disintegration.

In the Figure 18b, the model PA shows that the most solicited part of the block was the intersection between its face shells and webs. It happens because the mortar is under high confinement in this region, preventing displacements of the central portion of the mortar joint to both sides. This phenomenon did not occur in the model PO, in which the ratio of mortar and blocks' modulus of elasticity and the friction developed between the components are not sufficient to maintain a high confining pressure at the central portion of the mortar joint. To understand better this effect, the mortar's stress state will be checked.

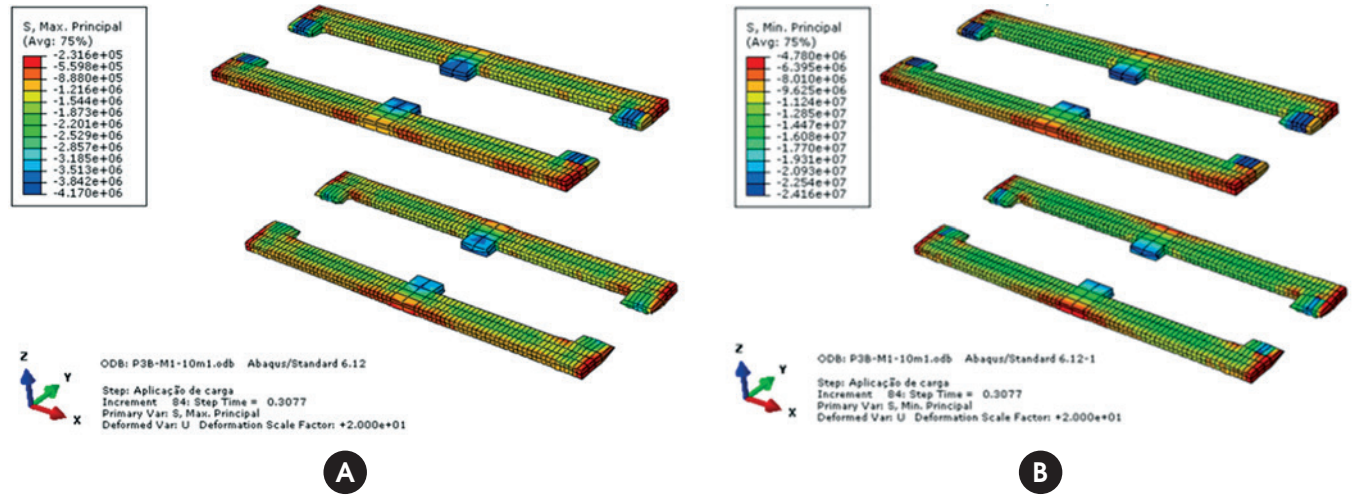

Figure 19
a) Maximum principal stress; b) Minimum principal stress – both numerically obtained, in Pa – only mortar: PO model

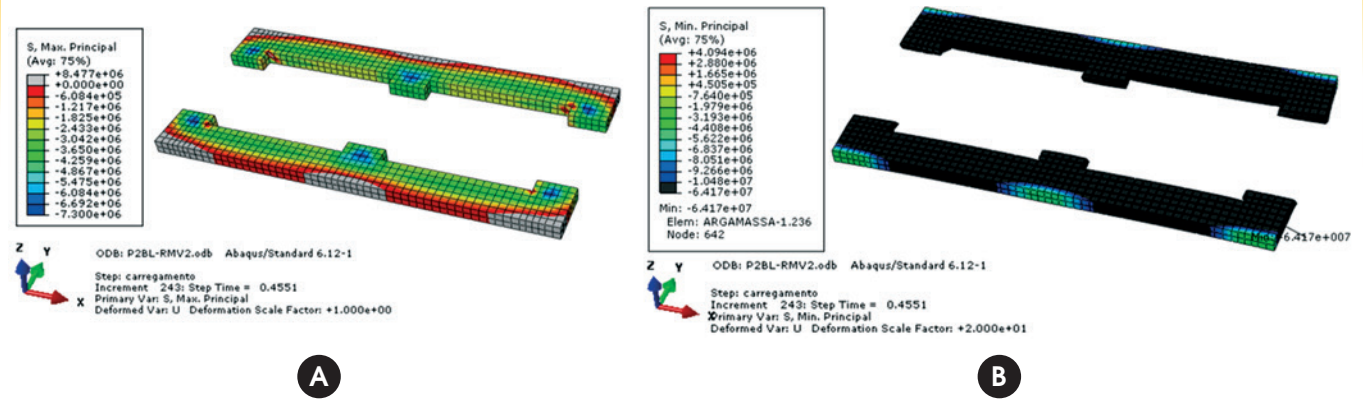

Figure 20
a) Maximum principal stress; b) Minimum principal stress – both numerically obtained, in Pa – only mortar: PA model

4.3 Principal stresses in the mortar joints

In Figure 19ab and Figure 20ab, the principal stresses in the mortar joints are presented, for the models PO and PA.
Analyzing the Figure 19a (model PO), it is possible to observe that mortar is completely compressed in its two directions due to the confining effect. In the model PA (Figure 20a), the mortar joint is not completely subjected to a triaxial state of compression, since its external part is subjected to a 0.9 MPa tensile stress. Then, the mortar is under low confinement in this region of the joint. This effect was not realized in the model PO, due to the lower ratio of mortar and blocks' modulus of elasticity ($E_{arg} / E_b = 0.375$).
Based on Figure 19b, all the mortar joint points were subjected to compressive stresses higher than the compressive strength obtained from the uniaxial compression test (PO – 3.52 MPa). The same behavior was observed in the Figure 20b, where all the black area corresponds to stresses higher than those obtained in the uniaxial compression test (PA – 11.80 MPa). In both cases this situ-

Table 11
Failure envelopes, PO – Mortar

		Comparison	Comparison	Comparison	
f_a[1] (MPa)	f_{tm} (MPa)	f_a* (MPa)	f_a* (MPa)	f_a* (MPa)	f_{tm}[2] (MPa)
3.52	1.00	6.12	5.82	24.16	11.40
	2.50	10.02	9.27		
	5.00	16.52	15.02		
	7.50	23.02	20.77		
	10.00	29.52	26.52		
	12.50	36.02	32.27		

[1] The uniaxial compressive strength of mortar was experimentally obtained by Oliveira (2);
[2] The confining strength was obtained by considering the average value of the vertical stresses acting close to the higher minimum principal stress, check (3).

Table 12
Failure envelopes, PA – Mortar

		Mohamad (3)	Khoo (4)	Numerical result	
f_a[1] (MPa)	f_{tm} (MPa)	f_a* (MPa)	f_a* (MPa)	f_a* (MPa)	f_{tm}[2] (MPa)
11.8	1.00	2.60	2.30	64.17	21.27
	5.00	13.00	11.50		
	10.00	26.00	23.00		
	15.00	39.00	34.50		
	20.00	52.00	46.00		
	35.00	91.00	80.50		

[1] The uniaxial compressive strength of mortar was experimentally obtained by Castro (1);
[2] The confining strength was obtained by considering the average value of the vertical stresses acting close to the lower minimum principal stress.

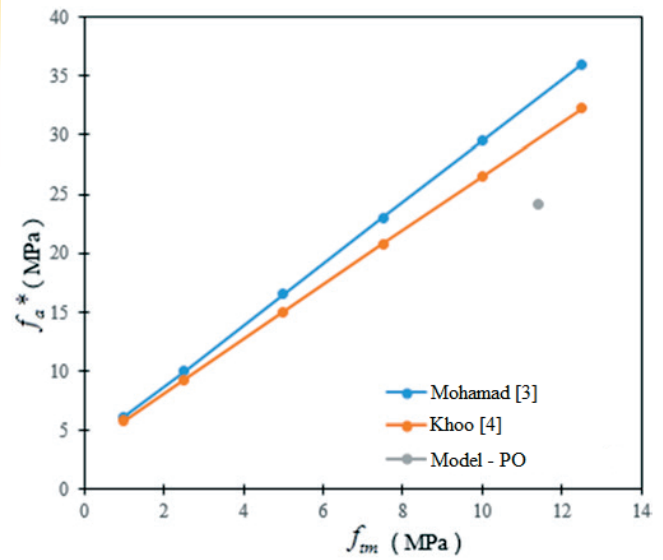

Figure 21
Rupture failure, PO – Mortar

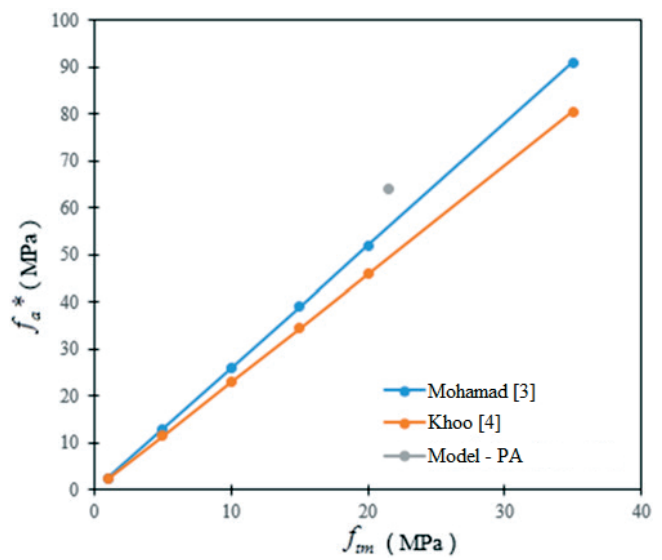

Figure 22
Rupture failure, PA – Mortar

ation is due to the confining effect, since the compressive strength of the material increases significantly when considering its actual triaxial stress state.

Assuming the equation (1) proposed by (Mohamad [3]) and the equation (2) obtained by (Khoo [4]), the failure envelope will be reproduced, in order to verify if the lower minor principal stress (obtained numerically) exceeds the envelope, at the rupture's load level. The main point is to verify if the confined mortar's crushing did happen.

Using the equations e knowing that the lower minor principal stress is equal to 24.16 MPa and 64.17 MPa, for PO and PA, respectively, the failure envelopes were built in Table 11 and Table 12, Figure 21 and Figure 22 show the failure envelopes for both studied models.

Considering Figure 21 and Figure 22, it is possible to affirm that at the time of the rupture, PO model presented the lower minor principal stress close to the maximum mortar's triaxial compressive strength. For PA model, the lower minor principal stress had already exceeded the two failure envelopes. Note that these envelopes, obtained by (Mohamad [3]) and (Khoo [4]), are only estimates. For better assessment, it is recommended to carry out studies about the mortar triaxial behavior, as those performed by the authors and [Oliveira 2]. However, their failure envelopes can be considered as tools to assist in the determination of possible failure modes.

4.4 Avaliation of failure modes

Based on the itens 4.2 and 4.3, it is possible to say that the rupture of prisms PO occurred due to a combination of factors. They presented large flexural cracks in their walls, and also block and mortar crushing. The transverse block splitting was the more evident rupture mode in the experimental test. Comparing the model proposed by (Chema e Klinger [8]) at the item 2.3 to the results obtained numerically, the ratio $E_{arg} / E_b = 0.375$ would indicate a block's tensile failure, which was verified in the numerical analysis.

In PA model, at the time of the rupture, some points of the mortar had already exceeded its compressive strength under confining pressure, causing the localized crushing of the mortar joint. This behavior was observed in some points of the prisms during the research. According to (Chema e Klinger [8]), the localized crushing of the mortar can cause some stress concentration, leading to the appearance of block's cracks by compression. Figure 17 indicates that the blocks' lower minor principal stress exceeded the value of their uniaxial compression strength, indicating the localized crushing in the blocks.

Thus, the failure mode of PA prism consisted of the simultaneous occurrence of webs rupture, due to the bending caused by the face shell mortar bedding (inducing tensile stresses), and localized crushing of the mortar joint, which induced blocks' localized crushing. Comparing the model proposed by (Chema e Klinger [8]) with the numerical results, for the ratio $E_{arg} / E_b = 0,46$ (indicated in the item 2.3) the rupture would be given by a block's tensile failure. This behavior was also obtained in the numerical analysis.

5. Conclusions

Based on the presented results, it is possible to conclude that numerical models are able to reproduce the mechanical behavior and the failure mechanisms of prisms of ordinary and high strength concrete blocks. The difference between the compressive strength and the modulus of elasticity obtained numerically and experimentally was around 3% for the PO model and 5% for the PA model.

In addition, the rupture of PO and PA prisms occurred due to a combination of factors. Block's web tensile failure happened in both of the models, due to the face shell mortar bedding, and was the most significant failure mode of both experimental and numerical point of view.

Although both models showed the bending effect on the flanges, each one presented some peculiarities when achieved the maximum supported load, due to the mechanical properties of its own components.

In the PO model, the friction developed between block and mortar was enough to keep the mortar completely confined. However, in the imminence of block's crushing resulted of the localized crushing of the mortar, the transverse block splitting occurred.

In the PA model, the region close to the inner face of the blocks presented a localized crushing of the mortar followed by the localized crushing of the blocks. In the outer face, there were tensile stresses in both block and mortar, due to the expulsion of the mortar. Such effect was not observed in the PO model, due to the lower ratio of the mortar and block's modulus of elasticity.

6. Acknowledgements

The authors thank the Brazilian agencies Research Support Foundation of Minas Gerais (FAPEMIG) and Coordination for the Improvement of Higher Education Personnel (CAPES), and also the Departament of Civil Engineering of the Federal University of Vicosa, for the support provided to this study.

7. References

[1] CASTRO, L. O. Avaliação experimental da interação de paredes de blocos de concreto de alta resistência sob ações verticais. 2015. Dissertação (mestrado) – Universidade Federal de Viçosa, Viçosa, 2015.

[2] OLIVEIRA, L. M. F. Estudo teórico e experimental do comportamento das interfaces verticais de paredes interconectadas de alvenaria estrutural. 2014. 272f. Tese (Doutorado), Escola de Engenharia de São Carlos, São Paulo, 2014.

[3] MOHAMAD, G. Mecanismos de ruptura da alvenaria de blocos à compressão. 2007. 290f. Tese (Doutorado), Escola de Engenharia, Universidade do Minho, Portugal, 2007.

[4] KHOO, C.L. A failure criterion for brickwork in axial compression. Ph.D. Thesis, University of Edinburgh, Edinburgh, Scotland, 1972.

[5] RIDDINGTON, J. R., FONG, K. H.; JUKES, P. Numerical study of failure initiation in different joint shear tests. University of Sussex. Masonry international Journal, vol, 11, Nº 2, 1997.

[6] HAMID, A. A.; DRYSDALE R. G. Suggested failure criteria for grouted concrete masonry under axial compression. American Concrete Institute- Journal Proceedings. Vol. 76 (n. 10):1047-1062. Out. 1979.

[7] ROMAGNA R. H. Resistência à compressão de prismas de blocos de concreto grauteados e não grauteados. 2000. 195f. Dissertação (Mestrado), Universidade Federal de Santa Catarina, Florianópolis, Santa Catarina, 2000.

[8] CHEEMA, T.S.; KLINGNER, R. E. Compressive strength of a concrete masonry prism. American Concrete Institute Journal. January-February, 1986. p. 88-97.

[9] JUSTE, A.E. Estudo da resistência e da deformabilidade da alvenaria de blocos de concreto submetida a esforços de compressão. 2001. 255f. Dissertação (Mestrado), Escola de Engenharia de São Carlos, São Paulo. 2001.

[10] KMIECIK P.; KAMINSKI, M. Modelling of Reinforced Concrete Structures and Composite Structures with Concrete Strength Degradation Taken Into Consideration. Archives of Civil and Mechanical Engineering, vol. Vol.-XI, No. 3, 2011.

[11] LUBLINER J., OLIVER J., OLLER S, OÑATE E. A plastic-damage model for concrete, International Journal of Solids and Structures. Vol. 25, 1989, pp. 299–329.

[12] GUO, Zhenhai. Principles of Reinforced Concrete. 1ª edição. Oxford, Elsevier, 2014. 587 f.

[13] SIMULIA Software ABAQUS 6.12. Dassault Systèmes, USA, 2012.

[14] CARDOSO, H. S (2014). Estudo Teórico-Experimental de Parafusos Utilizados como Dispositivos de Transferência de Carga em Pilares Mistos Tubulares Preenchidos com Concreto. Dissertação (Mestrado). Escola de Engenharia, Universidade Federal de Minas Gerais, Belo Horizonte, 2014.

[15] AGUIAR, O. P. Estudo do comportamento de conectores Crestbond em pilares mistos tubulares preenchidos com concreto. 230 f. Escola de Engenharia, Universidade Federal de Minas Gerais, Belo Horizonte, 2015.

[16] COMITÉ EURO-INTERNATIONAL DU BETÓN. CEB-FIP mode code 2012. Bulletin d'Information, 2012.

[17] ASSOCIAÇÃO BRASILEIRA DE NORMAS TÉCNICAS. NBR 6118:2014 – Projetos de estrutura de concreto - procedimentos. Rio de Janeiro, 2008.